connecting fluid channels (continuous-phase flow resistance r) between two data-carrying channels (continuous-phase flow resistance R, with $r > R$). A single bubble traversing the ladder is slowed down by flow through the alternate path. When both bubbles are present simultaneously, there is a net flow from the channel with the leading bubble to the one with the lagging bubble, creating a relative velocity gradient until the bubbles are synchronized (fig. S3).

Because bubble logic chips have no moving parts, they can be fabricated in a wide variety of materials, including silicon and glass, that are compatible with reaction chemistries unsuitable for PDMS channels. Moreover, because they operate at low Reynolds and capillary numbers, further reduction in size is feasible with faster switching times. The device mechanisms do not depend on non-Newtonian fluid properties; hence, matching dimensionless flow parameters will allow bubble logic circuits to be designed using different fluids, such as water droplets in oil or oil droplets in water.

The universal logic gates, toggle flip-flop, ripple counter, synchronizer, ring oscillator, and electro–bubble modulator presented here exhibit nonlinearity, bistability, gain, synchronization, cascading, feedback, and programmability. Having shown the required properties of a scalable logic family, they can be used to create complex microfluidic circuits capable of performing arbitrary fluid process control and computation in an integrated fashion. Such circuits may reduce the size, cost, and complexity of current microfluidic systems, thereby enabling the development of very-large-scale microfluidic reactors for use in areas including combinatorial chemistry and drug discovery. These bubble logic processors, where a bit of information can also carry a chemical payload, merge chemistry with computation.

References and Notes

1. M. A. Unger, H.-P. Chou, T. Thorsen, A. Scherer, S. R. Quake, *Science* **288**, 113 (2000).
2. T. Thorsen, S. J. Maerkl, S. Quake, *Science* **298**, 580 (2002); published online 26 September 2002 (10.1126/science.1076996).
3. C. C. Lee *et al.*, *Science* **310**, 1793 (2005).
4. F. K. Balagaddé, L. You, C. L. Hansen, F. H. Arnold, S. R. Quake, *Science* **309**, 137 (2005).
5. K. Jensen, A. Lee, *Lab Chip* **4**, 31N (2004).
6. B. Zheng, L. S. Roach, R. F. Ismagilov, *J. Am. Chem. Soc.* **125**, 11170 (2003).
7. P. R. C. Gascoyne *et al.*, *Lab Chip* **4**, 299 (2004).
8. D. Link *et al.*, *Angew. Chem. Int. Ed.* **45**, 2556 (2006).
9. M. Joanicot, A. Ajdari, *Science* **309**, 887 (2005).
10. Y.-C. Tan, J. S. Fisher, A. I. Lee, V. Cristini, A. P. Lee, *Lab Chip* **4**, 292 (2004).
11. G. Cristobal, J.-P. Benoit, M. Joanicot, A. Ajdari, *Appl. Phys. Lett.* **89**, 034104 (2006).
12. O. Steinbock, P. Kettunen, K. Showalter, *J. Phys. Chem.* **100**, 18970 (1996).
13. G. Seelig, D. Soloveichik, D. Y. Zhang, E. Winfree, *Science* **314**, 1585 (2006).
14. A. Conway, *A Guide to Fluidics* (Macdonald, London, 1972).
15. C. A. Belsterling, *Fluidic Systems Design* (Wiley Interscience, New York, 1971).
16. A. Groisman, M. Enzelberger, S. R. Quake, *Science* **300**, 955 (2003).
17. A. Groisman, S. R. Quake, *Phys. Rev. Lett.* **92**, 094501 (2004).
18. T. Vestad, D. W. Marr, T. Munakata, *Appl. Phys. Lett.* **84**, 5074 (2004).
19. E. Fredkin, T. Toffoli, *Int. J. Theor. Phys.* **21**, 219 (1982).
20. H. Chang, Ed., *Magnetic Bubble Technology: Integrated-Circuit Magnetics for Digital Storage and Processing* (IEEE Press, New York, 1975).
21. F. Jousse, G. Lian, R. Janes, J. Melrose, *Lab Chip* **5**, 646 (2005).
22. F. P. Bretherton, *J. Fluid Mech.* **10**, 166 (1961).
23. H. Wong, C. Radke, S. Morris, *J. Fluid Mech.* **292**, 95 (1995).
24. C. W. Park, *Phys. Fluids* **4**, 2335 (1992).
25. D. Link, S. Anna, D. Weitz, H. Stone, *Phys. Rev. Lett.* **92**, 054503 (2004).
26. M. J. Fuerstman, P. Garstecki, G. M. Whitesides, *Science* **315**, 828 (2007); published online 4 January 2007 (10.1126/science.1134514).
27. T. Thorsen, R. W. Roberts, F. H. Arnold, S. R. Quake, *Phys. Rev. Lett.* **86**, 4163 (2001).
28. P. Garstecki *et al.*, *Appl. Phys. Lett.* **85**, 2649 (2004).
29. T. Ward, M. Faivre, M. Abkarian, H. Stone, *Electrophoresis* **26**, 3716 (2005).
30. M. He, J. S. Kuo, D. T. Chiu, *Appl. Phys. Lett.* **87**, 031916 (2005).
31. Surface energy for a bubble trapped in a channel was evaluated from photomicrographs captured by a high-speed camera (Phantom V5.0, Vision research, minimum exposure time 10 μs). The grayscale images from the camera were digitized, a threshold filter was applied, and an edge detector was used to locate the bubbles and find their perimeter.

32. Supported by the MIT Center for Bits and Atoms (NSF grant CCR-0122419).

Supporting Online Material
www.sciencemag.org/cgi/content/full/315/5813/832/DC1
Figs. S1 and S2
Movies S1 to S6

30 October 2006; accepted 5 January 2007
10.1126/science.1136907

Chemical and Spectroscopic Evidence for an Fe^{V}-Oxo Complex

Filipe Tiago de Oliveira,[1]* Arani Chanda,[1]* Deboshri Banerjee,[1] Xiaopeng Shan,[2] Sujit Mondal,[1] Lawrence Que Jr.,[2]† Emile L. Bominaar,[1]† Eckard Münck,[1]† Terrence J. Collins[1]†

Iron(V)-oxo species have been proposed as key reactive intermediates in the catalysis of oxygen-activating enzymes and synthetic catalysts. Here, we report the synthesis of $[Fe(TAML)(O)]^{-}$ in nearly quantitative yield, where TAML is a macrocyclic tetraamide ligand. Mass spectrometry, Mössbauer, electron paramagnetic resonance, and x-ray absorption spectroscopies, as well as reactivity studies and density functional theory calculations show that this long-lived (hours at −60°C) intermediate is a spin S = 1/2 iron(V)-oxo complex. Iron-TAML systems have proven to be efficient catalysts in the decomposition of numerous pollutants by hydrogen peroxide, and the species we characterized is a likely reactive intermediate in these reactions.

High-valent iron-oxo intermediates are used in biological systems to carry out challenging oxidations in many scenarios (*1*–*3*). It has long been known that heme-based systems, biological as well as synthetic, do not attain the iron(V) state. Rather, the so-called "Compound I" intermediate involves the Fe^{IV}(oxo)(porphyrin-radical-cation), $Fe^{IV}(O)(P^{+\bullet})$, which is well established in peroxidases and catalases and presumed with considerable justification to be the reactive oxidizing species of the cytochrome P450s (*1*). Recently, Newcomb and co-workers reported laser flash photolysis experiments of an iron-corrole complex (*4*) and cytochrome P450 mutant CYP 119 (*5*), in which optically detected transients were tentatively assigned to Fe^{V}-oxo species. Que and co-workers, on the basis of ^{18}O labeling experiments, have postulated that an HO-Fe^{V}-oxo oxidant is an intermediate in the large family of Rieske dioxygenase enzymes (*3*). Iron(V) complexes are exceedingly rare, but recently, Wieghardt and co-workers reported spectroscopic evidence for a non-heme S = 1/2 iron(V)-nitrido complex produced by photolysis of an azidoiron(III) precursor (*6*).

Tetraamido macrocyclic ligands (TAMLs) can stabilize a variety of high-valent iron complexes, including a high-spin (S = 2) iron(IV) complex, intermediate-spin (S = 1) iron(IV) complexes, oxo-bridged diiron(IV) dimers, and an S = 1 iron(III)(TAML-radical-cation) complex [all reviewed in (*7*)]. The structurally characterized oxo-bridged complex, $[(Fe^{IV}B^{*})_2(\mu\text{-oxo})]^{2-}$, **2**, (B*, a TAML, is shown in Fig. 1) was obtained by reacting the monomeric iron(III) precursor, $[Fe^{III}B^{*}(H_2O)]^{-}$, **1**, with air (*8*). Fe-TAML activation of peroxide has been shown to be useful in numerous applications (*9*, *10*). The deprotonated TAML (a tetraanion) presents the iron with four exceptionally strong amido-N σ-donors. Therefore, it has been reasonable to expect (*11*) that this macrocyclic ligand would be capable of stabilizing an oxo-iron(V) complex when an Fe^{III}(TAML) complex is treated with an oxygen-atom transfer agent such as peroxide. A variety of iron(IV) complexes have been synthesized by reacting iron(II) precursors with oxygen donors

[1]Department of Chemistry, Carnegie Mellon University, Pittsburgh, PA 15213, USA. [2]Department of Chemistry and Center for Metals in Biocatalysis, University of Minnesota, Minneapolis, MN 55455, USA.

*These authors contributed equally to this work.
†To whom correspondence should be addressed. E-mail: que@chem.umn.edu (L.Q.); eb7g@andrew.cmu.edu (E.L.B.); emunck@cmu.edu (E.M.); tc1u@andrew.cmu.edu (T.J.C.)

Downloaded from http://science.sciencemag.org/ on January 20, 2017

in organic solvents such that the reaction can be monitored optically at temperatures as low as –80°C (*12*, *13*). A similar approach was applied here to Fe^{III} precursors to monitor short-lived intermediates in the reactions of TAML complexes. We report the synthesis of a d^3 iron(V)-oxo complex, in nearly quantitative yield, and its characterization with optical, electron paramagnetic resonance (EPR), Mössbauer, and x-ray absorption spectroscopies, as well as electrospray ionization mass spectrometry (ESI-MS), reactivity studies, and density functional theory (DFT).

The reaction of $[PPh_4][Fe^{III}B^*(H_2O)]$ (**1**, 1 to 2 mM) with 2 to 5 equivalents (equiv) of *m*-chloroperbenzoic acid (*m*CPBA) at –60°C in *n*-butyronitrile (*14*) produces within about 10 s the diiron(IV) dimer, **2** (Fig. 1, dotted line). The reaction then proceeds through an as-yet uncharacterized EPR-silent Fe(IV) intermediate (a Mössbauer spectrum is shown in fig. S3) to yield, within 15 min after the addition of *m*CPBA, a deep green species, **3**. Complex **3** (Fig. 1, solid line) exhibits distinct absorption maxima at 445 nm (where the extinction coefficient, ε, is 5400 M^{-1} cm^{-1}, calibrated by reference to Mössbauer spectra) and 630 nm (ε = 4200 M^{-1} cm^{-1}). At –60°C, **3** decays by 10% in 90 min, but it is stable for at least one month at 77 K. Complex **3** was also obtained in acetonitrile at –40°C, but at this temperature it decays by 10% in about 5 min, probably by attacking the solvent (*11*). In the course of our studies, we learned that **3** can be obtained quantitatively with 1 equiv of *m*CPBA when small amounts of potential ligands such as water, pyridine, and benzoic acid were present. The spectral features of **3** were independent of the presence of these potential ligands.

ESI-MS examination of *n*-butyronitrile solutions of **3** revealed one prominent ion at a mass-to-charge ratio (m/z) of 442.2, the mass and isotopic distribution pattern of which correspond to a formulation of $[Fe^{V}B^*(O)]^-$ [see supporting online material (SOM) text and fig. S1]. Only one other peak was observed, at m/z = 581.1, and it corresponded to a decay product of **3**, namely $[Fe^{IV}B^*(m\text{-chlorobenzoate})]^-$. Introduction of $H_2{}^{18}O$ into the solvent media yielded up to 35% of $[Fe^{V}B^*(^{18}O)]^-$ (m/z = 444.2) after 30 min of incubation; presently, we do not know at what stage of the reaction the ^{18}O exchange occurs.

In the 28 K EPR spectrum of **3** (Fig. 2A, solid line), prepared at −60°C in the glass-forming solvent, *n*-butyronitrile, the major feature belongs to an $S = 1/2$ species with *g* values of about 1.99, 1.97, and 1.74. [*g* values are the eigenvalues of tensor **g**, which couples the electronic spin, **S**, to the applied magnetic field, **B** (Eq. 1).] The dashed line represents a spectral simulation, drawn to correspond to an $S = 1/2$ spin concentration of 0.92(5) (estimated error from spectral simulation in the least significant digit) spins per Fe molecule. A minor species, present in all samples, with $g_1 = g_2 = 2.06$ and $g_3 \approx 2.00$ to 2.02 contributes about 3% of the total spin concentration.

We studied samples of **3** with Mössbauer spectroscopy between 4.2 and 140 K in applied magnetic fields up to 8.0 T. Three representative spectra of a sample prepared at −60°C are shown in Fig. 2B; additional spectra are displayed in fig. S2. The majority species contributes nearly 95% of the absorption, and thus we associate it with the majority $S = 1/2$ species observed by EPR. The Mössbauer spectra of **3** were simulated with the $S = 1/2$ spin Hamiltonian

$$H = \beta \mathbf{S}\cdot\mathbf{g}\cdot\mathbf{B} + \mathbf{S}\cdot\mathbf{A}\cdot\mathbf{I} - g_N\beta_N\mathbf{B}\cdot\mathbf{I} + (eQV_{zz}/12)[3I_z^2 - 15/4 + \eta(I_x^2 - I_y^2)] \quad (1)$$

In Eq. 1, β is the Bohr magneton; **S** is the electron spin operator; **g** is the *g* tensor; **B** is the applied magnetic field; **A** is the ^{57}Fe magnetic hyperfine tensor; **I** is the nuclear spin operator; $g_N\beta_N$ is the nuclear gyromagnetic ratio; I_x, I_y, and I_z are the Cartesian components of **I**; and the last term describes the interaction between the nuclear quadrupole moment *Q* and the electric field gradient (EFG) tensor [principal components V_{xx}, V_{yy}, V_{zz}; $\Delta E_Q = (eQV_{zz}/2)\sqrt{1+\eta^2/3}$ with $\eta = (V_{xx} - V_{yy})/V_{zz}$].

At 4.2 K, the electronic spin of **3** relaxes slowly on the time scale of Mössbauer spectroscopy (about 10^{-7} s), and thus we observed paramagnetic hyperfine structure. At 140 K, the spin system approaches the fast relaxation limit, and the magnetic hyperfine interactions were essentially averaged out. The spectrum i of Fig. 2B exhibits a doublet (solid line) with quadrupole splitting $\Delta E_Q = 4.25$ mm/s and isomer shift δ = −0.46(2) mm/s (relative to Fe metal at 298 K); δ = −0.42(3) mm/s at 4.2 K. This δ value is considerably lower than the lowest δ observed for any Fe-TAML complex, specifically δ = −0.18 mm/s (at 4.2 K) for an $S = 1$ iron(IV) complex (table S5). Because **3** has a half-integral electronic spin, we assigned this species to a low-spin d^3 $[Fe^{V}B^*(O)]^-$ complex, in accord with the mass spectroscopic data. The solid lines in Fig. 2B are spectral simulations based on Eq. 1 according to the parameters listed in Table 1. The theoretical curves in ii and iii in Fig. 2B represent 95% of the total Fe in the sample, in excellent agreement with the EPR data [0.92(5)] spins per Fe molecule].

Structural evidence for the nature of **3** derives from x-ray absorption spectroscopic studies at the Fe K edge. (The Fe K edge corresponds to the transition of the iron 1 s electron to the continuum of electron states.) A sample in frozen CH_3CN solvent, 70% pure in **3**, exhibits a K edge at 7125.3 eV, an energy value 1.4 eV higher than that associated with its iron(III) precursor **1** and thus consistent with the higher oxidation state of **3**. The 1s → 3d pre-edge transition found for the sample of **3** is quite intense, with an area of 48 units compared with 17 units for **1** (Fig. 3A). Taking into account that only 70% of the sample is **3** [the remainder being Fe(IV)], a pre-edge area of at least 60 units can be estimated for

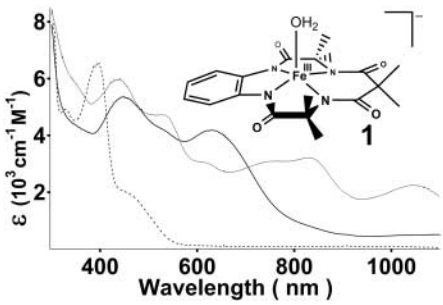

Fig. 1. Electronic absorption spectra of **1** (dashed line) and of **2** (dotted line) and **3** (solid line) as they formed during a reaction in *n*-butyronitrile at –60°C by the addition of 3 equiv of *m*CPBA. The inset shows the iron(III)-aqua complex **1**, $[Fe^{III}B^*(H_2O)]^-$, where the free-base H_4B^* tetraamide is 3,3,6,6,9,9-hexamethyl-3,4,8,9-tetrahydro-1H-1,4,8,11-benzotetraazacyclotridecine-2,5,7,10(6H,11H)-tetraone.

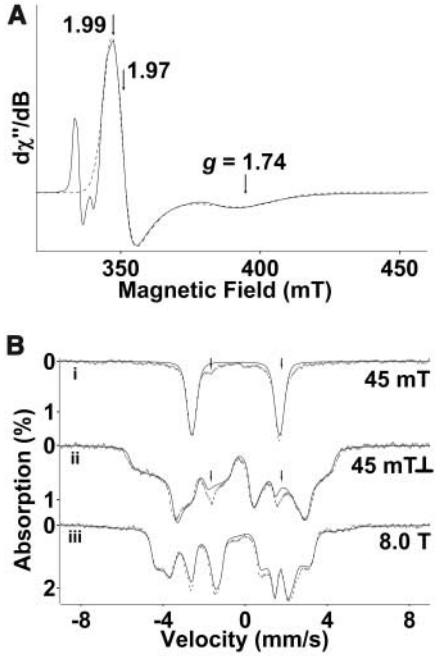

Fig. 2. (**A**) X-band EPR spectrum of about 2 mM ^{57}Fe-enriched **3** in *n*-butyronitrile. Conditions: T = 28 K; frequency, 9.66 GHz; microwave power, 0.02 mW; modulation, 1 mT. The dashed line is a spectral simulation for the majority species, **3**, using the following parameters: $g_x = 1.985$, $g_y = 1.966$, $g_z = 1.735$, with *g* values assumed to have a Gaussian distribution with $\sigma_{g_x} = 0.02$, $\sigma_{g_y} = 0.03$, and $\sigma_{g_z} = 0.05$, using a packet width of 1 mT. The *y* axis of the EPR spectrum is expressed in arbitrary units. (**B**) Mössbauer spectra of about 2 mM ^{57}Fe-enriched $[Fe^{V}B^*(O)]^-$, **3**, in *n*-butyronitrile recorded at 140 K (i) and 4.2 K (ii and iii) in magnetic fields indicated; incident γ beam perpendicular (ii) and parallel (i and iii) to the applied field. The solid lines are spectral simulations based on Eq. 1 using the parameters of Table 1; as drawn they represent 95% of the total absorption. Arrows (in i and ii) indicate a decay product (3% of Fe) of **3** with ΔE_Q = 3.4 mm/s and δ = 0.08 mm/s.

Downloaded from http://science.sciencemag.org/ on January 20, 2017

pure **3**. This value is distinctly larger than those observed for known $S = 1$ six-coordinate oxo-iron(IV) species (25 to 38 units) (*12*).

Direct evidence for an iron-oxo unit is obtained from an analysis of the extended x-ray absorption fine structure (EXAFS) region of the x-ray absorption spectrum (Fig. 3B). The best fit obtained considers three shells: 0.7 O scatterer (fixed on the basis of the Mössbauer analysis of this sample) at 1.58 Å, four N/O scatterers at 1.87 Å, and five C scatterers at 2.82 Å (see SOM text for details of the fitting protocol). Whereas the scatterers at 1.87 and 2.82 Å are consistent with low Z atoms from the macrocyclic ligand as found in the EXAFS fits for **1**, the 1.58 Å scatterer is unique for **3** and assigned to the oxo atom of an Fe-O unit. Thus, **3** can be formulated as $[Fe^{V}B^{*}(O)]^{-}$ by a combination of evidence from electrospray mass spectrometry, EPR, Mössbauer analysis, and x-ray absorption spectroscopy.

Consistent with the above formulation, **3** displays the signature reactivity features of a strongly oxidizing iron-oxo complex. Thus, reaction of excess triphenylphosphine (10 equiv) with preformed **3** [1 mM in 500:1 volume by volume acetonitrile to water, with the use of 1 equiv of *m*CPBA at –40°C] quantitatively produced triphenylphosphine oxide (1 mM $OPPh_3$), regenerating **1**. When this reaction was carried out in the presence of $H_2{}^{18}O$ (0.2% by volume), incorporation of ^{18}O in the oxidized product was observed by gas chromatography–mass spectrometry studies. As described in the SOM text (table S3), oxidation proceeded readily with other substrates under similar conditions, also showing ^{18}O incorporation when $H_2{}^{18}O$ was present. Thioanisole was oxidized quantitatively to the corresponding sulfoxide. Substoichiometric reactions with styrene and cyclooctene produced the corresponding epoxides; reaction with ethylbenzene gave a mixture of 1-phenylethanol and acetophenone. In these cases where **3** did not revert completely to iron(III), a mixture of lower-valent iron complexes was produced, including the diiron(IV) dimer, **2**. Oxidation of 9,10-dihydroanthracene proceeded quantitatively to anthracene and **2**.

Table 1. Mössbauer, EPR, and DFT parameters of $[Fe^{V}B^{*}(O)]^{-}$. Numbers in parentheses indicate the estimated errors in the least significant digits. Because DFT calculations generally produce contact terms that are too small (isotropic), the A values were obtained by adding the calculated spin-dipolar contribution to the experimental $A_{iso} = (A_x + A_y + A_z)/3$ and then adding a correction for the orbital contribution as described in the SOM text.

	g_x, g_y, g_z	$(A_x, A_y, A_z)/g_N\beta_N$(T)	ΔE_Q(mm/s)	η	δ(mm/s)
Exp	1.99, 1.97, 1.74	−49.3(10), −1.5(15), −16.3(15)	+4.25(10)	0.65(10)	−0.42(3)*
DFT	–	−43.6, −9.5, −15.0	+4.51	0.72	−0.39

*At 4.2 K relative to Fe metal at 298 K.

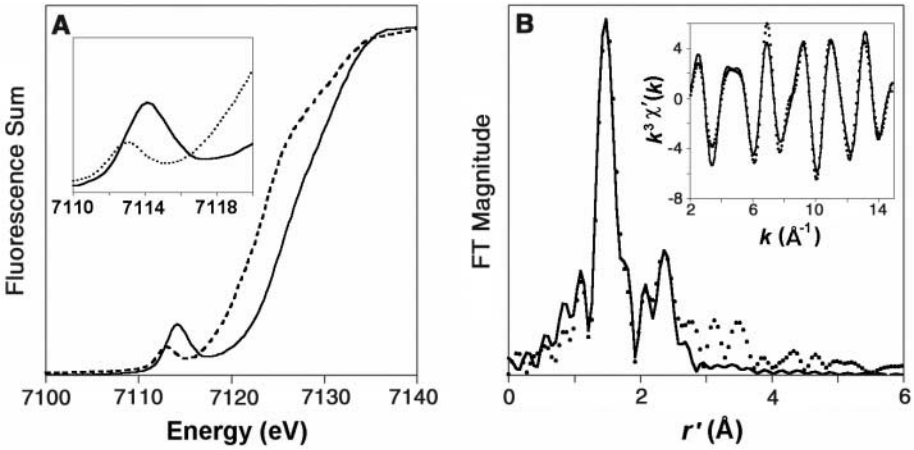

Fig. 3. (**A**) X-ray absorption near-edge spectra (Fe K edge) of **3** (solid line) and **1** (dashed line). The inset shows the magnified 1s → 3d transition features. (**B**) Fourier transforms of the Fe K edge EXAFS data ($k^3\chi(k)$) (dots) and the fit (solid line) for **3** with 0.7 O scatterer at 1.58 Å, four N/O scatterers at 1.87 Å, and five C scatterers at 2.82 Å. The inset shows Fourier-filtered EXAFS spectra ($k^3\chi'(k)$) (dots) and the fit (solid line). Fourier transform range k = 2 to 14.9 Å^{-1}; back-transform range: r' = 0.70 to 3.00 Å. The fitting protocol is detailed in SOM text.

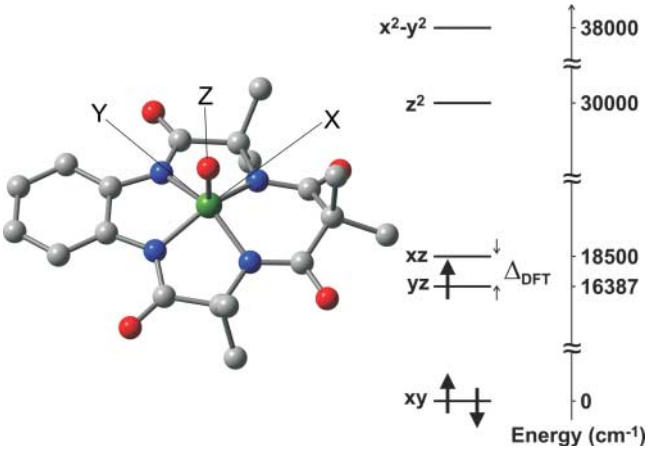

Fig. 4. Geometry-optimized structure of **3** as obtained from DFT calculations (green, iron; red, oxygen; blue, nitrogen; and gray, carbon). For clarity, hydrogen atoms are not shown. Electronic d-orbital diagram of the Fe^{V} center is shown, as derived from DFT. Selected bond lengths: Fe–O, 1.60 Å; Fe–N, 1.86 Å (two nitrogens along x direction) and 1.91 Å (two nitrogens along y direction); the Fe is 0.5 Å above the plane defined by the four amide nitrogens.

DFT calculations using Gaussian with the functional B3LYP and basis set 6-311G clearly favor the low-spin (S = 1/2) $[Fe^{V}B^{*}(O)]^{-}$ configuration as the ground state of **3**. A geometry-optimized structure together with an orbital diagram is shown in Fig. 4. The calculated Fe-O bond length of 1.60 Å is in excellent agreement with our EXAFS results. This distance is 0.04 to 0.1 Å shorter than those reported for Fe^{IV}=O complexes (*13*). The contraction of the Fe-O bond reflects an increase in the formal bond order from 2 in Fe^{IV}=O to 2.5. The Fe atom is displaced out of the 4-N plane by 0.5 Å. DFT calculations showed the lowest excited S = 3/2 state to be an Fe^{IV}-TAML cation radical state, $[Fe^{IV}(B^{*})^{+\bullet}(O)]^{-}$, at 1900 cm^{-1} rather than the metal-based state obtained by a spin flip transition from xy to xz (*15*).

One-electron oxidations of iron-oxo-porphyrinates are generally ligand based rather than metal based as in **3** (*16*). A major factor contributing to this difference is the stronger σ-donor capacity of the deprotonated amide nitrogens of a TAML tetraanion compared with the pyrroles of the porphyrin dianion. Hence, the TAML injects more electronic charge into the 3d shell than does a porphyrin, thereby raising the energy of the redox-active metal orbital and protecting the iron(V) against electron transfer from the phenyl moiety.

The values calculated for δ, ΔE_Q, η, and $A_{x,y,z}$ (Table 1) provide strong support to our iron(V) assignment. The isomeric shift calculated for $[Fe^{V}B^{*}(O)]^{-}$, δ = −0.39 mm/s, is in excellent agreement with the data and is substantially lower than that calculated for $[Fe^{IV}(B^{*})^{+\bullet}(O)]^{-}$, δ = −0.15 mm/s (calculated δ values for Fe-TAML complexes agree within 0.02 to 0.03 mm/s with the experimental values; see table S5). The removal of a 3d electron (reducing the shielding of the nuclear charge) and the shortening of the Fe-O bond distance (enhancing the covalent 4s population) each increase the electron density at

Downloaded from http://science.sciencemag.org/ on January 20, 2017

the Fe nucleus, thus decreasing δ. In contrast, the removal of an electron from the redox-active ligand orbital has a minor effect on δ (e.g., δ = −0.15 mm/s for $[Fe^{IV}(B^*)^{+\bullet}(O)]^-$ compared with δ = −0.12 mm/s for $[Fe^{IV}(B^*)(O)]^{2-}$) (table S5). Inspection of the DFT results shows that the Fe-O bond of **3** has nearly the same covalency as the Fe-O bonds in Fe^{IV}=O complexes (*12*, *17*, *18*). The calculated unpaired spin density on the oxo group of **3** is 0.22, which is less than expected (≈0.4) by comparison with Fe^{IV}=O complexes (≈0.8); the difference can be traced to a spin polarization of the bonding ($p_x + d_{xz}$) orbital. The exchange potential generated by the d^{α}_{yz} electron places the virtual d^{α}_{xz} level below the d^{β}_{xz} level. As a consequence, the transfer of electron density from p^{α}_x to d^{α}_{xz} is greater than from p^{β}_x to d^{β}_{xz}, resulting in a negative spin density in p_x, which, combined with the positive spin density for p_y (~0.4), yields a net spin density of less than 0.4.

The *z* axis of Eq. 1 parallels the Fe-O bond within 5°. The unpaired electron in the d_{yz} orbital produces a large negative *x* component of the spin-dipolar part of the *A* tensor, $A_{(s\text{-}d)i}/g_N\beta_N$ = (−24.4, +8.7, +15.7) T, and together with the isotropic contact term gives the larger *A* value along *x*. Owing to the large energy gaps between the narrowly spaced (d_{xz}, d_{yz}) pair and the other 3d levels, spin-orbit coupling acts primarily between d_{xz} and d_{yz} and produces (i) an effective *g* value $g_z = 2(1 - \zeta/\Delta)$ (g_x and g_y are not affected) and (ii) an orbital contribution to the magnetic hyperfine interaction, $A_{Lz}I_zS_z$, where $A_{Lz} = P(g_z - 2) \approx -13$ T. Substitution of $\zeta = 260\ cm^{-1}$ and $\Delta_{DFT} = 2000\ cm^{-1}$ gives the observed value g_z = 1.74 and A_{Lz} = −13 T (*19*).

Complex **3** thus appears to have a low-spin d^3 configuration in contrast to a recently described isoelectronic manganese(IV)-oxo complex (*20*), which is high spin, *S* = 3/2, by EPR criteria. Our particular interest in TAML-catalyzed reactions pertains to their proven potential in green chemistry. The present work provides an opportunity to elucidate elementary steps in the catalytic cycles of TAML activators by taking advantage of the high purity of **3**, with its various prominent spectroscopic signatures, as a stoichiometric reagent.

References and Notes

1. I. G. Denisov, T. M. Makris, S. G. Sligar, I. Schlichting, *Chem. Rev.* **105**, 2253 (2005).
2. E. I. Solomon *et al.*, *Chem. Rev.* **100**, 235 (2000).
3. M. Costas, M. P. Mehn, M. P. Jensen, L. Que Jr., *Chem. Rev.* **104**, 939 (2004).
4. D. N. Harischandra, R. Zhang, M. Newcomb, *J. Am. Chem. Soc.* **127**, 13776 (2005).
5. M. Newcomb *et al.*, *J. Am. Chem. Soc.* **128**, 4580 (2006).
6. N. Aliaga-Alcalde *et al.*, *Angew. Chem. Int. Ed.* **44**, 2908 (2005).
7. A. Chanda *et al.*, *J. Inorg. Biochem.* **100**, 606 (2006).
8. A. Ghosh *et al.*, *J. Am. Chem. Soc.* **127**, 2505 (2005).
9. D. Banerjee *et al.*, *Angew. Chem. Int. Ed.* **45**, 3974 (2006).
10. S. S. Gupta *et al.*, *Science* **296**, 326 (2002).
11. M. J. Bartos *et al.*, *Coord. Chem. Rev.* **174**, 361 (1998).
12. M. R. Bukowski *et al.*, *Science* **310**, 1000 (2005).
13. J.-U. Rohde *et al.*, *Science* **299**, 1037 (2003).
14. Materials and methods are available as supporting material on *Science* Online.
15. The 3d spin-flip transition $(d_{xy})^{\beta} \rightarrow (d_{xz})^{\alpha}$ is higher in energy than the ligand-to-metal transition $(\pi_p)^{\beta} \rightarrow (d_{xz})^{\alpha}$, where π_p is the redox-active orbital of the phenyl moiety, owing to the large $\{d_{xz}, d_{yz}\} - d_{xy}$ splitting.
16. J. T. Groves, *J. Inorg. Biochem.* **100**, 434 (2006).
17. A. Decker, M. D. Clay, E. I. Solomon, *J. Inorg. Biochem.* **100**, 697 (2006).
18. F. Neese, *J. Inorg. Biochem.* **100**, 716 (2006).
19. The free-ion value for the one-electron spin-orbit coupling constant ζ is 580 cm^{-1} (*21*). Given the high degree of covalency of **3**, the adopted ζ is not unreasonable. $P = 2\ g_N\ \beta\ \beta_N <r^{-3}>_{3d}$ has been taken as 50 T.
20. T. H. Parsell, R. K. Behan, M. T. Green, M. P. Hendrich, A. S. Borovik, *J. Am. Chem. Soc.* **128**, 8728 (2006).
21. J. Bendix, M. Brorson, C. E. Schaffer, *Inorg. Chem.* **32**, 2838 (1993).

22. The work was supported by NIH grants EB001475 (E.M.) and GM-38767 (L.Q.), the Heinz Endowments (T.J.C.), Environmental Protection Agency (grant RD 83 to T.J.C.), and the Heinz Foundation for the Teresa Heinz Scholars for Environmental Research award (to D.B.). XAS data were collected on beamline X3B at the National Synchrotron Light Source, which is supported by the U.S. Department of Energy and the National Institutes of Health. We also thank M. Costas and A. Ghosh for valuable suggestions.

Supporting Online Material
www.sciencemag.org/cgi/content/full/1133417/DC1
Materials and Methods
SOM Text
Figs. S1 to S3
Tables S1 to S6
References

3 August 2006; accepted 12 December 2006
Published online 21 December 2006;
10.1126/science.1133417
Include this information when citing this paper.

Downloaded from http://science.sciencemag.org/ on January 20, 2017

Small Phytoplankton and Carbon Export from the Surface Ocean

Tammi L. Richardson[1]* and George A. Jackson[2]

Autotrophic picoplankton dominate primary production over large oceanic regions but are believed to contribute relatively little to carbon export from surface layers. Using analyses of data from the equatorial Pacific Ocean and Arabian Sea, we show that the relative direct and indirect contribution of picoplankton to export is proportional to their total net primary production, despite their small size. We suggest that all primary producers, not just the large cells, can contribute to export from the surface layer of the ocean at rates proportional to their production rates.

Carbon export from the oceanic surface layer is controlled by biological transformations that occur within the pelagic food web (*1*, *2*). Autotrophic picoplankton (<2 μm in diameter) often dominate primary production in these regions but are believed to contribute relatively little to carbon export from surface layers because of their small sizes, slow sinking rates, and rapid utilization in the microbial loop. Large, rapidly sinking phytoplankton, such as diatoms, are believed to control carbon flux from upper ocean layers, and their contributions to export are believed to be disproportionately larger than their contributions to total primary production (*1*). Here we ask whether the contributions of picoplankton to carbon fluxes from the surface ocean are, in fact, disproportionately low.

Using results from inverse and network analyses of U.S. Joint Global Ocean Flux Study (JGOFS) data from the equatorial Pacific (EqPac) and Arabian Sea, we show that the relative contributions of various phytoplankton size classes to carbon export are proportional to their contributions to total net primary production (NPP) (*3*) (Fig. 1). Potential export pathways include direct routes, such as aggregation and incorporation into settling detritus, and indirect export through the consumption of picoplankton aggregates by organisms at higher trophic levels. The network analysis used in these studies (*4*) estimates the total particulate organic carbon (POC) flux that originated from each input source, here the NPP of each phytoplankton size class. In the EqPac, for example, picoplankton contributed 70% or more of the total NPP measured during JGOFS EqPac time series cruises and were responsible for 87% of POC export via detritus and 76% of carbon exported through the mesozooplankton (*5*). Mesozooplankton consumed both picoplankton-derived detritus and picoplankton-fed micrograzers. Similarly, at a northern station in the Arabian Sea during the Northeast Monsoon, picoplankton NPP was 86% of the total and was the source for 97 and 75% of the total carbon exported from the euphotic zone via the POC and mesozooplankton pathways, respectively (*6*). The relative contributions of the picoplankton to carbon export decreased where they produced relatively less of the total NPP but were nonetheless substantial (Fig. 1 and Table 1).

We believe that the contributions of picoplankton to carbon flux from oceanic surface layers have been overlooked because of assumptions that are made about cell size, sinking dynamics, and the trophic pathways of picoplankton through ecosystems. The seminal paper

[1]Marine Sciences Program and Department of Biological Sciences, University of South Carolina, Columbia, SC 29208, USA. [2]Department of Oceanography, Texas A&M University, MS 3146, College Station, TX 77843–3146, USA.

*To whom correspondence should be addressed. E-mail: richardson@biol.sc.edu

EXTENDED PDF FORMAT
SPONSORED BY

www.rndsystems.com

Science
AAAS

Chemical and Spectroscopic Evidence for an Fe^{V}-Oxo Complex

Filipe Tiago de Oliveira, Arani Chanda, Deboshri Banerjee, Xiaopeng Shan, Sujit Mondal, Lawrence Que Jr., Emile L. Bominaar, Eckard Münck and Terrence J. Collins (December 21, 2006)

Science **315** (5813), 835-838. [doi: 10.1126/science.1133417]
originally published online December 21, 2006

Editor's Summary

This copy is for your personal, non-commercial use only.

Article Tools Visit the online version of this article to access the personalization and article tools:
http://science.sciencemag.org/content/315/5813/835

Permissions Obtain information about reproducing this article:
http://www.sciencemag.org/about/permissions.dtl

Science (print ISSN 0036-8075; online ISSN 1095-9203) is published weekly, except the last week in December, by the American Association for the Advancement of Science, 1200 New York Avenue NW, Washington, DC 20005. Copyright 2016 by the American Association for the Advancement of Science; all rights reserved. The title *Science* is a registered trademark of AAAS.

Downloaded from http://science.sciencemag.org/ on January 20, 2017